JOURNAL OF COMPUTATIONAL PHYSICS 73, 148–167 (1987)

The Two-Dimensional Adiabatic Relaxation Method for MHD Modelling

JAMES W. EASTWOOD

Culham Laboratory, Abingdon, Oxon, OX14 3DB, United Kingdom
(EURATOM/UKAEA Fusion Association)

Received February 3, 1986; revised May 9, 1986

The adiabatic relaxation method is extended to two dimensions using a moving finite element model. The MHD equations are split into ideal and diffusion parts by employing a fractional timestep. The ideal equations are expressed in variational form using Hamilton's principle. Finite element discretisation of the variational principle leads to equations for studying equilibria, time dependent MHD and stability It is shown that conjugate gradient accelerated SSOR is effective in solving the nonlinear minimisation problem arising in finding equilibria. Aligning the finite elements with flux surfaces causes surface averaged transport to emerge naturally from the diffusion part of the timestep. © 1987 Academic Press, Inc.

1. INTRODUCTION

The complexity of the motion of a plasma confined by a magnetic field has led to a large variety of simulation models [1]. Even in the MHD limit, the range of timescales is such that MHD models specifically designed for fast (Alfvenic), mixed (resistive), and slow (transport) timescales have been developed. The longest timescale is that of an equilibrium, the stability of which to ideal MHD modes is investigated by computing eigenvalues and eigenvectors of the linearised fast timescale equations [3, 23, 26, 28].

Computer modelling of a MHD plasma remains a formidable task, so further simplifying assumptions are generally made. At one extreme are the one-dimensional transport codes [1, 4, 5], where simplifications are made by assuming a high degree of symmetry whilst retaining a detailed model of transport processes. Notable pioneering modelling of this type was that performed using the Hain–Roberts code [2]. Such models cannot predict effects of toroidal curvature, cross sections shaping, multiple magnetic axes, MHD stability, etc. At the other extreme are Eulerian multidimensional programs [1, 6, 7] which retain a limited description of the physics but allow more complicated field geometries.

A principal limitation of Eulerian calculations is numerical diffusion. A Lagrangian formulation overcomes this problem in one dimension but then runs into difficulties in two and three dimensions with the shear of the computational grid. The problems associated with purely Lagrangian and with purely Eulerian schemes has led a number of investigators to develop mixed Euler–Lagrange

0021-9991/87 $3.00

schemes in an effort to get the best of both approaches, for example, PIC methods [8], ICED-ALE [9], and the Waterbag method [10, 11, 12]. The MHD Waterbag method treats principal coordinate surfaces—the flux surfaces—in a Lagrangian fashion and employs an orthogonalisation procedure for the placement of points on those surfaces. This approach is effective for single magnetic axis systems and forms the basis of the $1\frac{1}{2}$D transport code G2M [13].

The adiabatic relaxation method described in this paper owes its origin to the adiabatic relaxation [5, 16] and Waterbag [10] methods devised by Keith Roberts. The study was initially motivated by the need to investigate geometrical effects, multiple axes, etc. in pinch simulation studies. One objective was to get a unified approach which would allow the same numerical representation to be used for equilibrium, stability, and transport studies. That such an objective can be achieved with the adiabatic relaxation method has, I believe, been demonstrated. Any success here owes much to the guiding influence of Keith Roberts, who took an active interest and made many constructive suggestions throughout the studies reported here.

Two principal features of the adiabatic relaxation method are that residual errors arising from not iterating to exact solutions are physical in nature (an unknown kinetic energy), and that finite elements, rather than finite differences are used in its discretisation. These two factors lead to schemes which are both robust and flexible. The efficacy of the finite element formulation is widely recognised in the solution of the Grad–Shafranov equation of equilibria, in the study of the stability of such equilibrium, and in the solution of three-dimensional equilibria [3, 22, 23, 24, 26, 28]. In the finite element implementation described herein, an arbitrary triangular mesh of piecewise linear elements is used (cf. [14]). Unlike finite difference counterparts, no particular element connectivity is assumed, so local rezoning and refinement can be performed to handle local shears and reconnection in evolutionary calculations; this procedure is similar to that used successfully in free Lagrangian methods for hydrodynamics [25].

The next section gives the equations and Section 3 discusses the relaxation and equilibrium problem using triangular elements. The remainder of the paper discusses linear properties, ideal MHD, and surface-averaged transport.

2. The Equations

We take as our starting point the charge neutral multifluid MHD equations:

$$\frac{d\rho}{dt} + \rho \nabla \cdot \mathbf{u} = S_m \tag{1}$$

$$\rho \frac{d\mathbf{u}}{dt} + \nabla p - \mathbf{j} \times \mathbf{B} = 0 \tag{2}$$

$$\frac{nk_B}{\gamma-1}\frac{dT}{dt}+nk_BT\nabla\cdot\mathbf{u}=\nabla\cdot\underline{\kappa}\cdot\nabla T+S_e \tag{3}$$

$$\mathbf{E}+\boldsymbol{u}\times\mathbf{B}=\underline{\eta}\cdot\mathbf{j}, \tag{4}$$

where ρ, $\mathbf{u}$, p, $\mathbf{j}$, $\mathbf{B}$, n, T, S_m, S_e are respectively mass density, fluid velocity, pressure, current density, magnetic field, number density, temperature, and souces. The multifluid model repeats Eq. (3) for each species and takes p as the sum of partial pressures. For our present purposes, it is sufficient to consider a single fluid model, so

$$p=nk_BT. \tag{5}$$

Time derivatives appearing in Eqs. (1)–(4) are material derivatives:

$$\frac{d}{dt}\equiv\frac{\partial}{\partial t}+\mathbf{u}\cdot\nabla. \tag{6}$$

The fields satisfy Ampere's and Faraday's laws:

$$\nabla\times\boldsymbol{B}=\mu_0\mathbf{j};\qquad\nabla\cdot\mathbf{B}=0 \tag{7}$$

$$\nabla\times\mathbf{E}=-\partial\mathbf{B}/\partial t. \tag{8}$$

2.1. *Timestep Splitting*

The timestep in the adiabatic relaxation model comprises two parts: an adiabatic stage, where plasma and fields change according to ideal MHD, and a dissipative stage, where source and diffusion are taken into account. The equations given above may be formally expressed.

$$\dot{U}-L_1(U)=L_2(U)+S, \tag{9}$$

where L_1 contains "advective" terms and L_2 contains "diffusive" terms.

The diffusive part of the timestep solves

$$\dot{U}=L_2(U)+S \tag{10}$$

and the advective part solves

$$\dot{U}=L_1(U). \tag{11}$$

Equations (10) and (11) when applied once timestep give an integration scheme which is first-order accurate in time. Second-order accuracy can be obtained by symmetrising the splitting in time.

Explicitly writing Eq. (10) gives

$$\frac{\partial \rho}{\partial t} = S_m \tag{12}$$

$$\frac{nk_B}{\gamma - 1}\frac{\partial T}{\partial t} = \nabla \cdot \underline{\kappa} \cdot \nabla T + S_e \tag{13}$$

$$\frac{\partial \mathbf{B}}{\partial t} = -\nabla \times \underline{\eta} \cdot \mathbf{j}. \tag{14}$$

Equation (11) for the advective stage becomes

$$\frac{d\rho}{dt} + \rho \nabla \cdot \mathbf{u} = 0 \tag{15}$$

$$\rho \frac{d\mathbf{u}}{dt} + \nabla p - \mathbf{j} \times \mathbf{B} = 0 \tag{16}$$

$$\frac{d}{dt} p\rho^{-\gamma} = 0 \tag{17}$$

$$\frac{d\mathbf{B}}{dt} - \mathbf{B} \cdot \nabla \mathbf{u} + \mathbf{B}(\nabla \cdot \mathbf{u}) = 0. \tag{18}$$

3. Relaxation Problem

Equations (15)–(18) are those of ideal MHD. The kinematic equations (15), (17), and (18) can be integrated to give point differential expressions for mass, entropy, and flux conservation in terms of the Lagrangian displacement gradient matrix $\underline{\mathbf{D}}$. The result is

$$\rho = \rho_0 |D|^{-1} \tag{19}$$

$$p = p_0 |D|^{-\gamma} \tag{20}$$

$$\mathbf{B} = |D|^{-1} \underline{\mathbf{D}} \cdot \mathbf{B}_0, \tag{21}$$

where elements of $\underline{\mathbf{D}}$ are given by

$$D_{ij} = \frac{\partial x_i}{\partial x_{0j}} \equiv \delta_{ij} + \frac{\partial \xi_i}{\partial x_{0j}} \tag{22}$$

and

$$\mathbf{x}(\mathbf{x}_0, t) = \mathbf{x}_0 + \boldsymbol{\xi}(\mathbf{x}_0, t) \tag{23}$$

is the (time dependent) Lagrangian coordinate of the fluid element initially at position $\mathbf{x}_0$. $\mathbf{D}$ provides a pointwise description of the deformation of a small fluid element. Its volume $d\tau_0$ becomes $d\tau = |D|\, d\tau_0$ and area $d\mathbf{s}_0$ of its surface becomes $d\mathbf{s} = |D|\, d\mathbf{s}_0 \cdot \mathbf{D}^{-1}$ under displacements described by Eq. (23).

Equations (19)–(23) can be combined with Eq. (16) to give a single equation for the evolution of the displacement field ξ. However, for purposes of discretisation, it is preferable to use Hamilton's principle and express the dynamics using the Lagrangian

$$\begin{aligned} L &= \int d\tau \left[\frac{1}{2} \rho u^2 - \frac{p}{\gamma - 1} - \frac{B^2}{2\mu_0} \right] \\ &= \int d\tau_0 |D| \left\{ \frac{1}{2} \rho_0 \dot{\xi}_i \dot{\xi}_i - \frac{p_0 |D|^{-\gamma}}{\gamma - 1} - \frac{|D|^{-2} (\mathbf{D} \cdot \mathbf{B}_0)^2}{2\mu_0} \right\} \\ &= \int d\tau_0 l(\dot{\xi}_i, \xi_{i,j}), \end{aligned} \tag{24}$$

where the Lagrangian density, l, satisfies the Euler–Lagrange equations.

3.1. *Finite Element Discretisation*

The discrete analogue of the Euler–Lagrange equations is obtained by approximating the displacement fields in Eq. (24) by a restricted class of functions

$$\xi_i = W^n(\mathbf{x}_0)\, \xi_i^n(t) \tag{25}$$

and taking variations of the approximate Lagrangian with respect to the set of unknown (nodal) amplitudes $\{\xi_i^n\}$. The subscripts in Eq. (25) and in what follows indicate components, superscripts denote nodes, and sums are implied over repeated indices.

Substituting Eq. (25) into Eq. (24) gives the approximate Lagrangian

$$\tilde{L} = \frac{1}{2} \left(\int d\tau_0 \rho_0 W^n W^m \right) \dot{\xi}_i^n \dot{\xi}_i^m - U(\{\xi_i^n\}) \tag{26}$$

and Euler–Lagrange equations

$$M^{nm} \ddot{\xi}_i = -\partial U / \partial \xi_i^n. \tag{27}$$

Elements of the mass matrix M are given by the integral appearing in Eq. (26). Replacing the time derivatives in Eq. (27) by a finite difference gives a set of discrete equations describing the plasma motion.

The relaxation approach is most appropriate in the long timescale limit, where inertia becomes a small correction term. The equilibrium limit drops the inertia entirely to give the nonlinear set of equations

$$\partial U / \partial \xi_i^n = 0. \tag{28}$$

U may be Taylor expanded about the initial configuration

$$U = U_0 - \xi^p \cdot \mathbf{F}^p + \tfrac{1}{2}\xi^p \cdot \mathbf{K}^{pq} \cdot \xi^q + O(\xi^3). \tag{29}$$

$\mathbf{F}^p$ is the load vector and $\mathbf{K}$ is the stiffness matrix. Sufficiently close to a stable equilibrium, $\mathbf{K}$ will have positive eigenvalues, although for an arbitrary initial condition this will not be necessarily so. Consequently, a nonlinear solution method which can handle $\mathbf{K}$ with negative eigenvalues is needed (see Section 4.1).

4. Equilibrium Calculations

In this section, we shall consider the implementation of Eq. (28) for systems with one ignorable coordinate. For simplicity, we present the discussion for a Cartesian system where z is ignorable ($\partial/\partial z \equiv 0$), and then indicate how other geometries may be tackled.

We require the minimum of the energy U,

$$U = \int d\tau_0 \left[\frac{p_0}{\gamma - 1} |D|^{1-\gamma} + |D|^{-2} \frac{(\mathbf{D} \cdot \mathbf{B}_0)^2}{2\mu_0} \right], \tag{30}$$

with respect to the Lagrangian displacement field, ξ. The displacement gradient matrix contains only first derivatives of ξ, so the lowest order conforming elements we can use are piecewise linear. Taking piecewise linear triangular elements causes components D_{ij} to be uniform over the elements and reduces Eq. (30) to the sum over the elements,

$$U = \Sigma \{ \Pi^0 |D|^{1-\gamma} + |D|^{-1} D_{\gamma\alpha} D_{\gamma\beta} \Gamma^0_{\alpha\beta} \}, \tag{31}$$

where for each element

$$\Pi^0 = \int \frac{d\tau_0 \, p_0}{\gamma - 1} \tag{32}$$

$$\Gamma^0_{\alpha\beta} = \int d\tau_0 \frac{B_{0\alpha} B_{0\beta}}{2\mu_0} \tag{33}$$

$$D_{ij} = \delta_{ij} + \lambda^n_j \xi^n_i. \tag{34}$$

The element side normal vector for side 1 is defined as

$$\boldsymbol{\lambda}^1 = (\mathbf{x}^3 - \mathbf{x}^2) \times \mathbf{e}_z / \Delta \tag{35}$$

and similarly for $\boldsymbol{\lambda}^2$ and $\boldsymbol{\lambda}^3$ by cyclically permuting indices in Eq. (35). $\mathbf{e}_z$ is the unit z-vector, Δ is the element area, and $(\mathbf{x}^1, \mathbf{x}^2, \mathbf{x}^3)$ are the positions of the element vertices, labelled anticlockwise. For z ignorable, the x and y components of Eq. (21) reduce to flux conservation, $\psi(x) = \psi_0(x_0)$. Representing p_0, ψ_0, and B_{0z} by

piecewise linear functions over the elements allows integrals in Eq. (32) and (33) to be evaluated, thus completing the discretisation of Eq. (31). If $\psi^2 = \psi^3$ is specified, then the elements are flux surface aligned as required for $1\frac{1}{2}D$ transport models.

4.1. *Energy Minimisation*

The starting point of an equilibrium calculation is an initial element triangulation with prescribed p, ψ, and B_z. The initial energy is $U^0 = \Sigma(\Pi^0 + \Gamma^0_{\alpha\alpha})$. After some displacement $\xi^{(1)}$, the energy becomes

$$U^1 \equiv U(\mathbf{x} + \xi^{(1)}) = \Sigma(\Pi^1 + \Gamma^1_{\alpha\alpha}),$$

where

$$\Pi^1 = \Pi^0 |D|^{1-\gamma}, \qquad \Gamma^1_{\alpha\alpha} = |D|^{-1} D_{\alpha\beta} D_{\alpha\gamma} \Gamma^0_{\beta\gamma}. \tag{36}$$

If $\xi^{(1)}$ is such that $U^1 < U^0$, then the move brings the configuration closer to equilibrium. A repeated application of this process defines an iterative process for computing an equilibrium:

repeat (1)–(3) until $\|F\| < \varepsilon$

(1) select $\xi^{(n+1)}$ such that $U^{n+1} < U^n$

(2) compute Π^{n+1}, $\Gamma^{n+1}_{\alpha\beta}$

(3) increment iteration counter, $n := n + 1$

In practice, poloidal and toroidal flux are stored instead of $\Gamma_{\alpha\beta}$.

The principal difficulty with this scheme is that of selecting the displacements $\{\xi\}$ to give a rapid monotonic decrease in U. The simplest approach is to search in the steepest descent direction, i.e., take $\xi^P = \alpha \mathbf{F}^P$. It then follows from Eq. (29) that for sufficiently small α, the search direction will guarantee $U^{n+1} < U^n$. However, if the stiffness matrix $\mathbf{K}$ is ill-conditioned, as is generally the case, the steepest descent will converge slowly.

The method that proved effective in one dimension was a nonlinear Newton iteration [16]. In this method, displacements at each step are found by solving the linearised problem $\mathbf{K} \cdot \xi = \mathbf{F}$. This gives quadratic convergence for $\mathbf{K}$ positive definite, but since positivity of $\mathbf{K}$ is not assured far from equilibrium, it can give quadratic divergence. In addition, to get quadratic convergence, the linearised problem must be solved exactly at each iteration.

A third possibility, and one which has proved most effective, is a preconditioned search algorithm. In the preconditioned search algorithm, the steepest descent direction $\mathbf{F}$ is replaced by the descent vector $\mathbf{M}^{-1} \cdot \mathbf{F}$, where $\mathbf{M}$ is some easily invertible approximation to the stiffness matrix $\mathbf{K}$. Both incomplete Choleski decomposition and SSOR decomposition were tried [17, 18, 29]: SSOR proved most effective and required less storage.

The definition and computation of load vector $\mathbf{F}$ and stiffness matrix $\mathbf{K}$ are as follows. Substituting Eq. (34) into Eq. (31) and expanding in terms of small $\{\xi\}$

yields an expression of the form Eq. (29). Each triangular finite element contributes to the three node vectors $\mathbf{F}^{p_1}$, $\mathbf{F}^{p_2}$, $\mathbf{F}^{p_3}$, where (p_1, p_2, p_3) are the address in the assembled load vector corresponding to nodes (1, 2, 3) of the element. Similarly, each element contributes a 3×3 submatrix $\delta\mathbf{K}^{p_i p_j}$ to the assembled stiffness matrix. In a straight Cartesian system, we find for each element that the contributions to the load vector are

$$\delta\mathbf{F}^p = \int d\tau_0 \left[\left(p_0 + \frac{B_0^2}{2\mu_0} \right) \boldsymbol{\lambda}^p - \frac{\mathbf{B}\cdot\boldsymbol{\lambda}^p}{\mu_0}\mathbf{B} \right] \tag{37}$$

and to the stiffness matrix are

$$\delta\mathbf{K}^{pq} = \int d\tau_0 \left[\left(\gamma p_0 + \frac{B_0^2}{\mu_0} \right) \boldsymbol{\lambda}^p\boldsymbol{\lambda}^q - \left(p_0 + \frac{B_0^2}{2\mu_0} \right) (\boldsymbol{\lambda}^p\boldsymbol{\lambda}^q - \boldsymbol{\lambda}^q\boldsymbol{\lambda}^p) \right.$$
$$\left. - \frac{1}{\mu_0} (\boldsymbol{\lambda}^p\mathbf{B}_0(\mathbf{B}_0\cdot\boldsymbol{\lambda}^q) + \mathbf{B}_0\boldsymbol{\lambda}^q(\mathbf{B}_0\cdot\boldsymbol{\lambda}^p)) + \frac{\mathbf{B}_0\cdot\boldsymbol{\lambda}^p\mathbf{B}_0\cdot\boldsymbol{\lambda}^q}{\mu_0}\mathbf{1} \right]. \tag{38}$$

Similar, but more complicated expressions arise for other geometries (see Section 4.2).

The algorithm for computing F and K is

1. clear global vector F and matrix K
2. do for each element
   - find $\delta\mathbf{F}$ and $\delta\mathbf{K}$
   - add $\delta\mathbf{F}$ to F
   - add $\delta\mathbf{K}$ to K

In the implementation, for an N-node system. F is a $3N\times 1$ vector and K is a $3N\times 3N$ sparse matrix. The preconditioning matrix M was formed either by zero infill incomplete Choleski decomposition [29],

$$M = LDL^{\mathrm{T}}, \tag{39}$$

where

$$L_{ij} = \begin{cases} K_{ij} = \sum_{k=1}^{j-1} L_{ik}D_kL_{jk} & K_{ij}\neq 0, \\ 0 & \text{otherwise}, \end{cases} \tag{40}$$
$$D_j = L_{jj}^{-1},$$

or, by SSOR decomposition [18], let

$$K = L + D + U, \tag{41}$$

then

$$M = (D + \omega L)\, D^{-1}(D + \omega U)/\omega(2 - \omega). \tag{42}$$

The positivity of the ICCG decomposition is not assured for this problem. If negative values of D_j are encountered, the decomposition is restarted with v added to the diagonals of K (v may be regarded as a pseudo-viscosity). The relaxation parameter ω for the SSOR decomposition was taken to be 1.7. Close to equilibrium when the ICCG decomposition remained positive, it gave fast convergence, but this was outweighed by the simplicity and robustness of SSOR decomposition. Both are implemented in the program described below, but the SSOR option was used for the examples given.

The preconditioned search scheme is as follows:

Outer Iteration.

(1) Compute stiffness matrix K and load vector F;

(2) approximate decomposition $M \doteq K$;

(3) compute initial search vector

$$s = M^{-1}F$$

$$\alpha_{\text{num}} = \langle F, s \rangle.$$

Inner Iteration.

(1) Compute distance to new minimum

$$\alpha_{\text{den}} = \langle s, Ks \rangle$$

$$\alpha = \alpha_{\text{num}}/\alpha_{\text{den}}$$

$$\xi = \xi + \alpha s;$$

(2) test new configuration,
compute F_{new};
if $\langle s, F_{\text{new}} \rangle > \varepsilon$, then line search until $\langle s, F_{\text{new}} \rangle < \varepsilon$;

(3) Compute new search direction

$$\beta_{\text{den}} = \alpha_{\text{num}}$$

$$\alpha_{\text{num}} = \langle F_{\text{new}}, M^{-1}F_{\text{new}} \rangle$$

$$\beta_{\text{num}} = \alpha_{\text{num}};$$

end if β_{num} sufficiently small

$$\beta = \beta_{\text{num}}/\beta_{\text{den}}$$

$$s = \beta s + N^{-1}F_{\text{new}}.$$

At each step, Π and Γ are updated by adjusting cell integrated pressure and magnetic fluxes according to Eqs. (36): This conserves entropy and flux. $\langle\ ,\ \rangle$ denotes the inner product: For vectors a and b of length $3N$, $\langle a, b\rangle = \sum_{r=1}^{3N} a_i b_i$.

When using in a transport model the start always remains close to equilibrium, and one outer iteration and a few inner iteration (~ 5) are sufficient to get a good equilibrium. However, when the calculation begins far from equilibrium, then a larger number of outer iterations may be required (cf. Section 5.1).

4.2. *Extensions of the Basic Problem*

The discussion so far pertains to a system in the absence of gravity or curvature effects. To include the effect of an externally imposed gravitational potential, $\phi(\mathbf{x})$, requires the addition of the term $\int \rho\phi\, d\tau$ to the energy functional. This leads to additonal first- and second-order contributions to the energy

$$\delta U_{\text{grav}} = \delta U_{0\,\text{grav}} + \int \rho_0 \xi \cdot \nabla_0 \phi_0\, d\tau_0 + \int \frac{\rho_0}{2} \xi_i \xi_j \frac{\partial^2 \phi_0}{\partial x_{0i}\, \partial x_{0j}}\, d\tau_0. \tag{43}$$

Equilibria in other geometries where there is an ignorable coordinate (e.g., toroidal or helical) are treated by transforming the Cartesian displacement gradient matrix into the appropriate coordinate system. For instance, suitable coordinates for the description of axisymmetric toroidal equilibria are polar coordinates $(v^1, v^2, v^3) = (R, \Phi, Z)$, where axisymmetric implies $\partial/\partial\Phi \equiv 0$. Triangular elements would then lie in the (R, Z) plane, and again the fields can be represented by two flux functions (ψ, RB_Φ).

In a general non-orthogonal system

$$U = \int \left[\frac{p}{\gamma - 1} + g_{mn} \frac{\bar{B}^m \bar{B}^n}{2\mu_0} \right] d\tau, \tag{44}$$

where $\bar{B}^k$ are contravariant field components. The kinematic conservation laws become

$$p = p_0 |D|^{-\gamma}, \qquad \bar{B}^k = |D|^{-1} C_l^k \bar{B}_0^l, \tag{45}$$

where

$$|D| = \frac{\partial(x, y, z)}{\partial(v^1, v^2, v^3)} \frac{\partial(v_0^1, v_0^2, v_0^3)}{\partial(x_0, y_0, z_0)} |C| \tag{46}$$

and

$$C_l^k = \partial v^k / \partial v_0^l.$$

The basic Cartesian description and implementation carry over to this more general case with only the addition of various metrics into the integrals. Indeed, the examples of Section 5 were all computed using the same program.

4.3. *Field Reconstruction*

During the iterative process for minimising the energy, only cell averaged quantities are updated in computing Π and Γ. Once the search for the new equilibrium is complete, then new piecewise linear approximations to the pressure and toroidal (z) fields are constructed by using weighted residual approximations to Eqs. (20) and (21). Pressure is given by solving

$$\int \phi(p - p_0 |D|^{-\gamma})\, d\tau = 0 \tag{47}$$

and z-magnetic field is given by

$$\int \phi(B_z - |D|^{-1} D_{3i} B_{0i})\, d\tau = 0. \tag{48}$$

If the elements are aligned with poloidal flux surfaces, then the basis functions ϕ can be chosen to be functions of ψ, reducing Eqs. (47) and (48) to one-dimensional equations for surface averaged p and B_z. In this case, Eq. (48) becomes a statement of surface z-flux conservation:

$$\int \phi B_z\, dA = \text{constant}.$$

In toroidal geometry, the z-magnetic field component is replaced by the covariant toroidal field component, $f = RB_\Phi$, and the toroidal version reduces to conservation of safety factor

$$\int \phi \frac{f}{R^2}\, d\tau = 2\pi \int \phi q\, d\psi = \text{constant}, \tag{49}$$

where, for example, $\phi(\psi)$ is taken to be a linear function.

5. Examples

An OLYMPUS [19, 20] Fortran program has been written implementing the arbitrary connectivity linear triangular finite element relaxation method in either straight or toroidal geometry and allowing for gravitational terms (Eq. (43)).

5.1. *Interchange Instability*

Figure 1 shows (a) the initial and (b) the equilibrium element triangulation and flux function. The initial state has gravity pointing downwards, $\mathbf{g} = -\mathbf{e}_y$, a density which increases with height, $\rho = 1 + y$, and a sheared magnetic field, $\mathbf{B} = (-y + \frac{1}{2}, 0, 1)$. Boundary conditions were of zero normal displacement at $y = 0$ and $y = 1$ and mirror symmetry about $x = 0$ and $x = 1$.

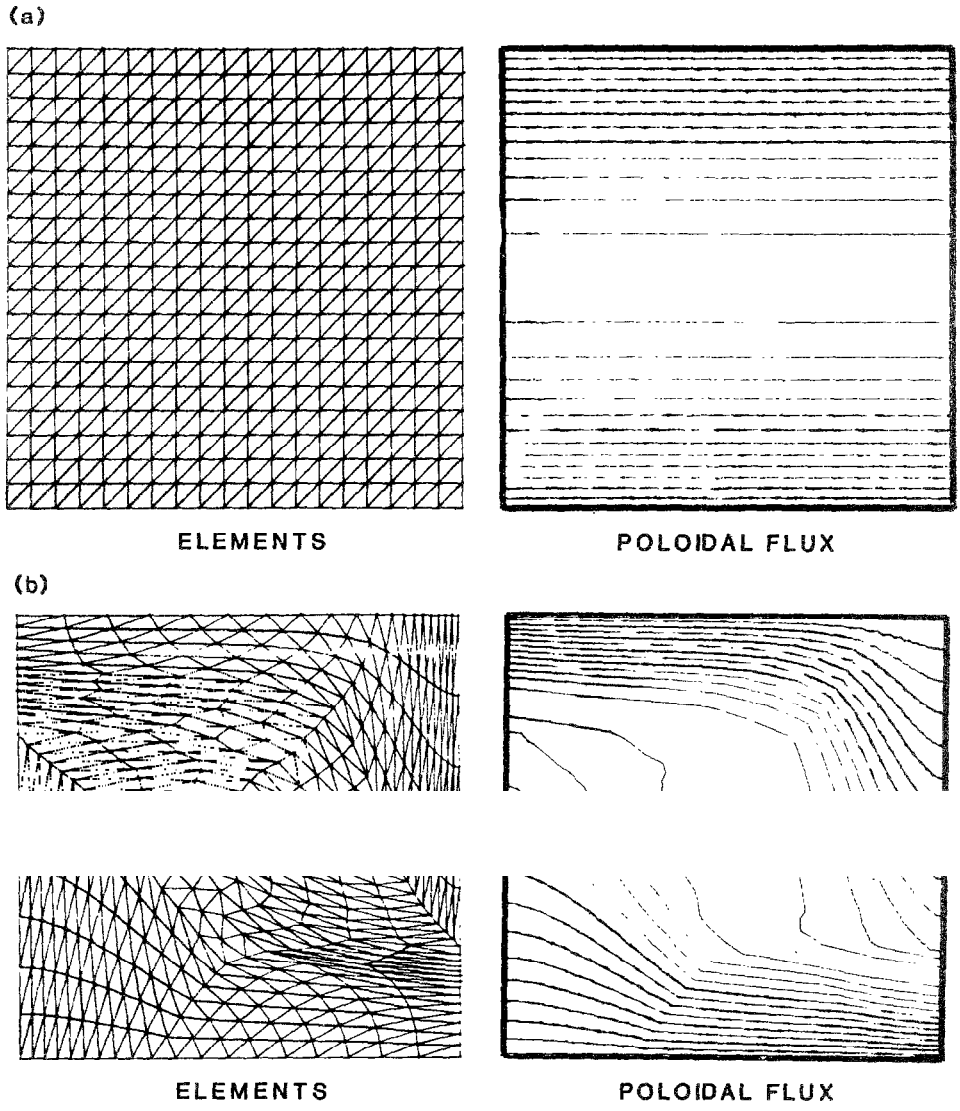

FIG. 1. (a) Initial and (b) equilibrium element triangulations and flux surfaces for the interchange instability in the presence of a sheared magnetic field.

Figure 2 shows the convergence of the nonlinear search algorithm for the case illustrated in Fig. 1. Ten inner iterations per outer iteration were used. The bad guess case corresponds to the node displacements shown in Fig. 1. In the good guess case, fields were reconstructed (cf. Section 4.3) to provide a new, near equilibrium, initial case. Timing for these calculations on an ICL 2976 computer are well approximated by the formula $(2 + n_{\text{out}}(14 + 5n_{\text{in}}))/8$ ms per element, where n_{out}

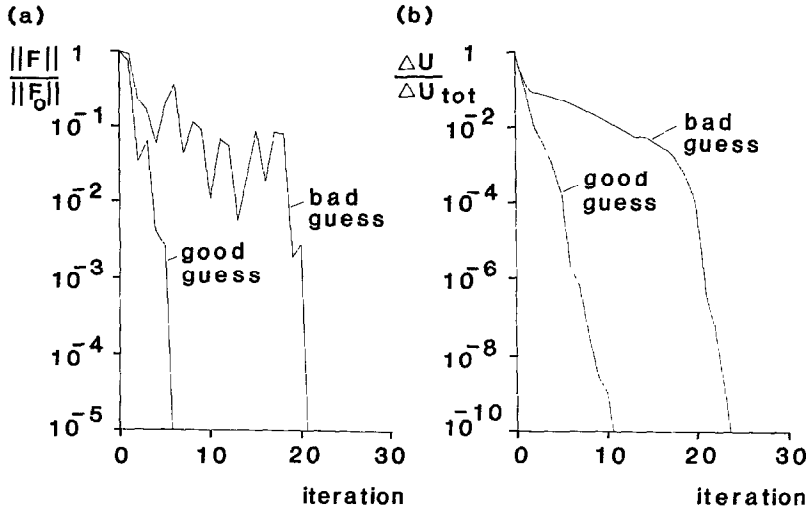

FIG. 2. The convergence of the nonlinear search algorithm when applied to the case shown in Fig. 1: (a) the residual force norm and (b) the difference of the residual energy from the equilibrium value. $\|F_0\|$ is the initial force norm and ΔU_{tot} is obtained by continuing iterations to roundoff.

and n_{in} are respectively the number of outer and inner iterations. Note that $\|F\|$ in Fig. 2a is not a monotonically decreasing function; this is due to the preconditioning.

5.2. *Toroidal Geometry*

Figure 3 illustrates (a) the initial element triangulation, (b) the initial pressure profile, (c) the equilibrium flux surfaces, and (d) mod B contours for a low beta reversed field pinch configuration. The initial pressure profile arises from taking parabolic density and temperature profiles and setting the axial β to 10^{-4}. Fields were initialised to have the same fluxes as the equivalent cylindrical Bessel function model:

$$\psi = rB_0 B_0 J_0(x)/x, \qquad f = (R_0^2 - r^2)^{1/2} B_0 J_0(x),$$

where $x = 2\theta r/a$, B_0 is field strength, a and R_0 are minor and major radii, and J_0 is the Bessel function. For $\theta = 1.4$, the equilibrium solver relaxes flux surfaces to the shapes shown in Fig. 3c. The mod B contours in Fig. 3d show about 50% trapping ratio on these surfaces.

Figures 4 and 5 are examples of the relaxation method applied to tokamak parameters. In both cases an aspect ratio of 3 and axial β of 2% are assumed, with initial pressure and safety factor profiles as shown in Fig. 4a. Pressures and safety factors are shown as fractions of axial pressure, p_0, and wall safety factor, $q_w = 4.8$. Initially, $f = RB_\Phi$ is set constant. Initial flux surfaces in both instances were taken to be nested toroidal surfaces with respectively circular and D-shaped cross section.

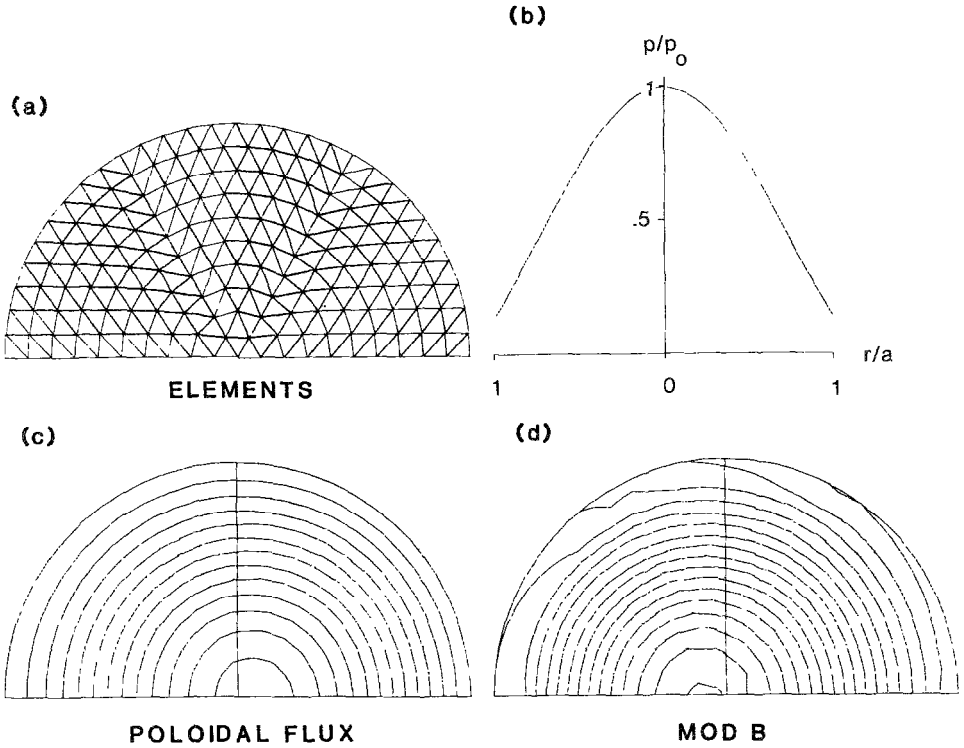

FIG. 3. (a) Initial element triangulation, (b) initial pressure profile, (c) equilibrium flux surfaces, and (d) $|B|$ contours for a low β RFP.

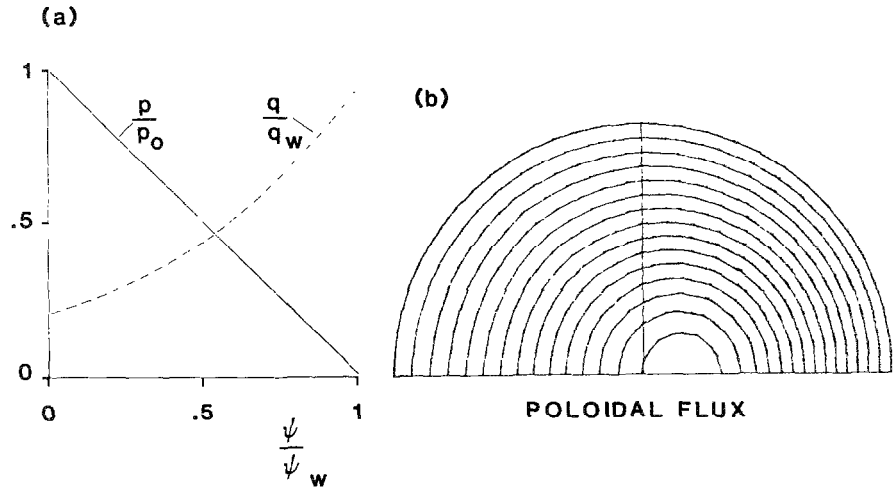

FIG. 4. (a) Initial pressure and safety factors as functions of poloidal flux and (b) equilibrium flux surfaces for an aspect ratio 3 circular cross section tokamak.

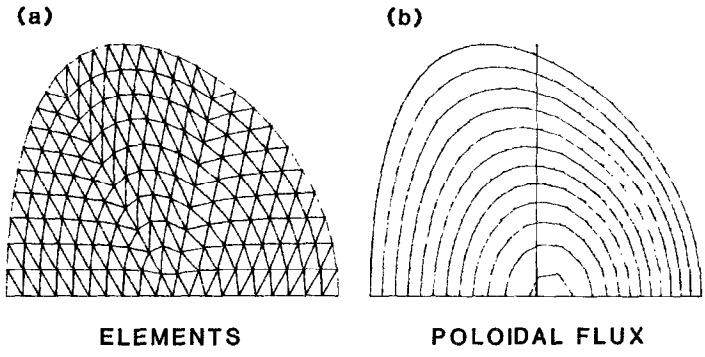

FIG. 5. (a) Initial element triangulation and (b) equilibrium flux surfaces for the same initial conditions as shown in Fig. 4a but applied to a D-shaped cross section.

Element triangulations used in both these cases were topologically equivalent to regular hexagonal meshes. The D-shaped surfaces in Fig. 5 were initialised to lie on surfaces where (R, Z) are given by

$$R = R_0 + r\cos(\theta + \delta \sin\theta)$$

$$z = \varepsilon r \sin\theta,$$

where elongation ε and skewness δ were given values $\varepsilon = 1.5$ and $\delta = 0.3$.

Figure 6 illustrates one advantage of the finite element approach: flexibility. Figure 6a shows a configuration with two magnetic axes, with local refinement of the element triangulation around the two axes. The tridiagonal solver which was used to reconstruct surface pressures and fluxes is in this case replaced by an incomplete Choleski decomposition conjugate gradient matrix solver. Even with such a physically singular problem the relaxation method converged, albeit to a configuration with large current densities near the x-point magnetic null. Note that

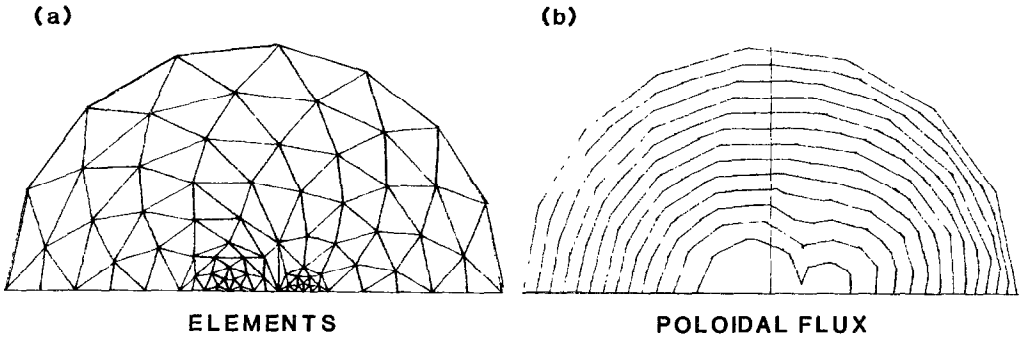

FIG. 6. (a) Element triangulation for a two-axis equilibrium and (b) flux surfaces after relaxation.

in the absence of transport, the topology of this configuration is fixed. Adding the transport step (Section 7) will allow nulls to decay, and reassembling the global matrices permits elements to be added, removed, or reconnected as required.

6. Ideal MHD

6.1. *Time Dependent*

Replacing the time derivative in Eq. (27) by finite differences in time gives the linear multistep scheme

$$M^t \qquad {}^{t+1}$$

where $F = -\partial U/\partial\xi$, superscripts indicate timelevel, and node and component indices have been omitted. If α^{t+1} is chosen to be zero, then Eq. (50) describes an explicit timestepping scheme whose timestep is restricted to Alfvén timescales.

A strongly implicit scheme is obtained by taking only α^{t+1} nonzero. In this case, we may write Eq. (50) as the equivalent minimum principle $\min_\xi[V]$, where

$$V = \left(\frac{\xi^{t+1} M^t \xi^{t+1} + U^{t+1}}{2\Delta t^2}\right) + \xi^{t+1} \frac{M^t}{\Delta t^2}(\xi^{t-1} - 2\xi^t)$$

and apply the equilibrium solver methods described above. This approach damps out high frequencies but still retains low frequency inertial effects which may be important, for instance, in long timescale modelling of fast pinches. In the limit of a large timstep, the equilibrium solver described earlier is recovered.

6.2. *Stability*

Linearising Eq. (27) and taking time dependence $\alpha \exp(i\omega t)$ yields the ideal MHD eigenvalue problem

$$\omega^2 M\xi = K\xi. \tag{51}$$

The method of obtaining the equilibrium described above ensures that Eq. (51) gives stable roots for axisymmetric modes. Stability to modes with z-dependence may be investigated by computing K for trial functions $\xi = W^n(x, y)\,\xi^n \exp(-ikz)$. Element triangulation, the method of matrix assembly and the structure of the resulting stiffness matrix are the same as for the equilibrium calculation, so problems of mixing different discretisation methods and interpolating from one mesh for equilibrium and to another for stability are absent.

It follows from the variational formulation that the eigenvalue ω^2 of the discrete problem bound those of the continuum from above. Thus, an unstable mode ($\omega^2 < 0$) in Eq. (51) is sufficient for one to exist there in the continuum. However,

for lower order elements, the convergence of the eigenspectrum of the discrete to the continuum model may be slow [3].

6.3. *Error Analysis*

A measure of the effect of finite element discretisation is provided by the dispersion relation for magnetosonic waves in a uniform plasma with uniform element triangulation (e.g., hexagonal). Evaluating Eq. (51) for ρ, p, and $\mathbf{B}$ uniform, assuming $\mathbf{k}$ and $\mathbf{b}$ lie in the plane of the elements, and Fourier transforming the resulting expression yields, after some algebra, the approximate Alfvén and two magnetosonic roots

$$\omega^2 = c_A^2 \mathbf{b}\cdot\mathbf{A}\cdot\mathbf{b}$$

$$\omega^2 = \mathrm{Tr}(\mathbf{A})\left\{\frac{c_A^2+c_S^2}{2} \pm \left[\left(\frac{c_A^2+c_S^2}{2}\right)^2 - c_A^2 c_S^2 \frac{\mathbf{b}\cdot\mathbf{A}\cdot\mathbf{b}}{\mathrm{Tr}(\mathbf{A})} - c_S^4 \frac{\det(\mathbf{A})}{\mathrm{Tr}(\mathbf{A})}\right]^{1/2}\right\}, \tag{52}$$

c_A, c_s, and $\mathbf{b}$ are respectively the Alfvén speed, sound speed, and unit vector along the unperturbed magnetic field. The matrix $\mathbf{A}$ is given by

$$\mathbf{A} = \sum_{n=\infty}^{\infty} |\tilde{W}(\mathbf{k}_n)|^2 \mathbf{k}_n \mathbf{k}_n / \Sigma_n |\tilde{W}(\mathbf{k}_n)|^2, \tag{53}$$

where $\tilde{W}$ is the fourier transform of the basis function W and $\mathbf{k}_n$ is the aliased wavenumber [21]. In the limit as element sizes tend to zero, $\mathbf{A} = \mathbf{kk}$, $\mathrm{Tr}(\mathbf{A}) = k^2$, $\det(\mathbf{A}) = 0$, and Eqs. (52) reduce to the usual Alfvén and magnetosonic roots.

Equations (52) and (53) show that the finite element model values of ω are always larger than the differential limit, ω_0, as expected from the variational formulation. The elements define preferred directions, so ω^2 depends not only on the relative directions of $\mathbf{b}$ and $\mathbf{k}$ but also on their orientations with respect to the element. In the special case of $\mathbf{k}$ aligned with a hexagonal mesh axis, the roots, ω, of Eqs. (52) differ from the correct values only by a multiplicative factor. For linear elements the factor gives a fractional error in the frequency

$$\Delta = \frac{\omega}{\omega_0} - 1 = \frac{3\sin^2\theta}{\theta^2(3-2\sin^2\theta)} - 1, \tag{54}$$

where $\theta = kH/2$, $|\theta| \leqslant \pi/2$, and H is the node spacing. Figure 7 shows Δ and the corresponding error arising if the mass matrix is lumped. To show the improvements to be expected by going to higher order, the corresponding curve for quadratic spline basis functions is shown. Note that whilst lumping leads to little deterioration for the case of linear elements, it has a dramatic effect on the higher order case.

A more general analysis of mesh effects on Eqs. (52) can be made by assuming a hexagonal mesh and evaluating the consequences of mesh shear and orientation. The conclusion from such an analysis is that wavelengths greater than four node

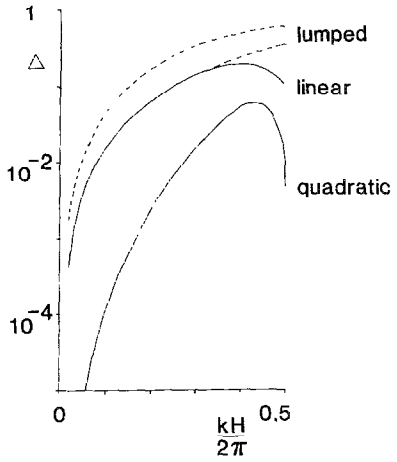

FIG. 7. Fractional errors in frequencies for Alfvén and magnetosonic waves for wavenumbers **k** aligned with a principal mesh axis. Solid curves are the errors for linear basis functions and quadratic splines. Corresponding curves when the mass matrix is lumped are shown by dashed lines. The upper curve is for lumped quadratic splines.

spacings are in general well approximated ($\leqslant 10\%$ error). Large mesh shear, giving obtuse triangular elements leads to rapid degradation of accuracy for shorter wavelengths. In addition, for arbitrary mesh orientations, the Alfvén root gives $\omega^2 > 0$ even when $\mathbf{k} \cdot \mathbf{b} = 0$ because of $n \neq 0$ terms in Eq. (53).

7. TRANSPORT MODELLING

Combining Eqs. (12)–(14) with the relaxation model for Eqs. (15)–(18) gives a self-consistent transport model. If elements are chosen to be aligned with flux surfaces, then on long timescales where density and temperature equilibrate on flux surfaces, the transport equations reduce to one-dimensional equations for surface averaged variables.

An obvious choice is elements which remain aligned with flux surfaces (cf. Section 4.3) but on which the value of poloidal flux can change to avoid elements accumulating at magnetic nulls. If we let the time dependent basis functions for the diffusion stage of the timestep be $\{\phi^s\}$ and the element velocity be **u**, then explicit reference to **u** in the discrete approximations to the surface equation is avoided by choosing "incompressible" surfaces, i.e., the surfaced average value $\langle \mathbf{u} \cdot \nabla \phi^s \rangle$ of $\mathbf{u} \cdot \nabla \phi^s$ is taken to be zero.

Consider, for example, the mass diffusion equation (12). This yields

$$\frac{d}{dt} \int \phi^s \rho \, d\tau = -\int \rho \mathbf{u} \cdot \nabla \phi^s \, d\tau + \int \phi^s S_m \, d\tau.$$

Writing $\rho = \rho^r \phi^r$, where ρ^r is the value of ρ on flux surface r and the sum over r is implied, and using the result $\langle \mathbf{u} \cdot \nabla \phi^s \rangle = 0$ reduces the projected mass diffusion equation to

$$\left\{ \int \phi^s \phi^r \, d\tau \right\} \frac{d\rho^r}{dt} = \int \phi^s S_m \, d\tau.$$

Similar simplifications occur for the temperature, poloidal, and toroidal flux equations. Replacing time derivatives by finite differences and assuming ϕ are piecewise linear functions reduces the transport equations to a set of block tridiagonal equations for single axis systems. For further details, see Ref. [15].

8. Final Remarks

The two-dimensional adiabatic relaxation method provides the basis for a consistent numerical approach to ideal MHD, stability, equilibrium, and transport calculations. Finite elements provide both accuracy nd flexibility. Matrix assembly permits local refinement and rezoning to allow field reconnection and to overcome the mesh shear problems that are inherent in two- and three-dimensional Lagrangian models. In addition, the local nature of the approximation enables a wide range of geometries and field connectivities to be tackled with the same software.

The relaxation method is robust in that residual errors may be interpreted physically as a residual (unknown) kinetic energy. It differs from the more commonly used Grad–Shafranov equation methods in that equilibria are found for prescribed flux surface entropy and safety factor rather than for prescribed pressure and toroidal flux functions. Also, it can be extended to include inertial corrections.

The implementation described combines three of Keith Roberts' ideas which have been influential in computational plasma physics: adiabatic relaxation, Lagrangian surface modelling ("waterbags"), and the OLYMPUS methodology and conventions for constructing scientific software. Hopefully, it will provide part of fitting tribute to his wide ranging computational physics interests and expertise.

Acknowledgments

I would like to express my thanks to the late Dr. K. V. Roberts who initiated the study reported here. The success of the project owes much to his ideas, interest, and constructive criticisms during the course of the work.

References

1. K. V. Roberts and D. E. Potter, *Methods Comput. Phys.* **9**, 339 (1970).
2. K. Hain, G. Hain, K. V. Roberts, and W. Köppendorfer, *Z. Naturforsch. A Phys. Phys. Chem. Kosmophys.* **15**, 1039 (1960).

3. R. GRUBER AND J. RAPPAZ, *Finite Element Methods in Linear Ideal Magnetohydrodynamics* (Springer-Verlag, New York/Berlin, 1985).
4. M. L. WATKINS, M. H. HUGHES, K. V. ROBERTS, P. M. KEEPING, AND J. KILLEEN, *Methods Comput. Phys.* **16**, 166 (1976).
5. J. P. CHRISTIANSEN AND K. V. ROBERTS, *Comput. Phys. Commun.* **14**, 423 (1978).
6. A. SYKES AND J. A. WESSON, *Phys. Rev. Lett.* **37**, 140 (1976).
7. D. SCHNACK AND J. KILLEEN, *J. Comput. Phys.* **35**, 110 (1980).
8. R. L. MORSE, *Methods Comput. Phys.* **9**, 213 (1970).
9. J. U. BRACKBILL, *Methods Comput. Phys.* **16**, 1 (1976).
10. H. L. BERK AND K. V. ROBERTS, *Methods Comput. Phys.* **9**, 87 (1970).
11. D. POTTER, *Methods Comput. Phys.* **16**, 43 (1976).
12. D. V. ANDERSON, *J. Comput. Phys.* **17**, 246 (1975).
13. R. N. BYRNE AND H. H. KLEIN, *J. Comput. Phys.* **26**, 352 (1978).
14. M. J. FRITTS AND J. P. BORIS, *J. Comput. Phys.* **31**, 173 (1979).
15. LEE-HSIAO AND J. W. EASTWOOD, *Culham Laboratory Report* CLM-R253, (HMSO, London, 1985).
16. K. V. ROBERTS, J. P. CHRISTIANSEN, AND J. W. LONG, *Comput. Phys. Commun.* **10**, 264 (1975).
17. J. W. EASTWOOD, Reading University Computer Science Report RCS67, 1977 (unpublished).
18. P. CONCUS, G. H. GOLUB, AND D. P. O'LEARY, *Sparse Matrix Computations*, edited by J. Bunch and D. Rose (Academic Press, New York/London, 1976), p. 309.
19. K. V. ROBERTS, *Comput. Phys. Commun.* **7**, 237 (1974).
20. M. H. HUGHES AND K. V. ROBERTS, *Comput. Phys. Commun.* **29**, 15 (1983).
21. R. W. HOCKNEY AND J. W. EASTWOOD, *Computer Simulation Using Particles* (McGraw-Hill, New York, 1981).
22. F. BAUER, O. BETANCOURT, AND P. GARBEDIAN, *A Computational Method in Plasma Physics* (Springer-Verlag, New York, 1978).
23. R. GRUBER, F. TROYON, AND D. BERGER, *Comput. Phys. Commun.* **21**, 323 (1981).
24. R. P. GUPTA, E. PANARELLA, AND P. SILVESTER, in *Int. Conf. on Plasma Physics: Joint Conf. on Plasma Theory 4th Kiev Conf. and the Warsaw and Lausanne Divisions 4th Int. Conf. N*
25. R. A. CLARK, in *Numer. Methods Fluid Dyn. II*, edited by K. W. Morton and M. J. Baines (Oxford Univ. Press, London, 1986).
26. M. S. CHANCE *et al. J. Comput. Phys.* **28**, 1 (1978).
27. G. STRANG AND G. FIX, *An Analysis of the Finite Element Method* (Prentice-Hall, Englewood Cliffs, N.J., 1973).
28. R. C. GRIMM, J. M. GREENE, AND J. L. JOHNSON, *Methods Comput. Phys.* **16**, 253 (1976).
29. J. A. MEIJERINK AND H. A. VAN DER VORST, *Math. Comput.* **31**, 148 (1977).